ARTICLE

How photocorrosion can trick you: A detailed study on low-bandgap Li doped CuO photocathodes for solar hydrogen production

Received 00th January 20xx,
Accepted 00th January 20xx

DOI: 10.1039/x0xx00000x

Jonathan Kampmann[a], Sophia Betzler[a,b], Hamidreza Hajiyani[c], Sebastian Häringer[a], Michael Beetz[a], Tristan Harzer[a], Jürgen Kraus[d], Bettina V. Lotsch[a,b], Christina Scheu[e], Rossitza Pentcheva[c], Dina Fattakhova-Rohlfing[f]* and Thomas Bein[a]*

The efficiency of photoelectrochemical tandem cells is still limited by the availability of stable low band gap electrodes. In this work, we report a photocathode based on lithium doped copper (II) oxide, a black p-type semiconductor. Density functional theory calculations with a Hubbard U term show that low concentrations of Li ($Li_{0.03}Cu_{0.97}O$) lead to an upward shift of the valence band maximum that crosses the Fermi level and results in a *p*-type semiconductor. Therefore, Li doping emerged as a suitable approach to manipulate the electronic structure of copper oxide based photocathodes. As this material class suffers from instability in water under operating conditions, the recorded photocurrents are repeatedly misinterpreted as hydrogen evolution evidence. We investigated the photocorrosion behavior of $Li_xCu_{1-x}O$ cathodes in detail and give the first mechanistic study of the fundamental physical process. The reduced copper oxide species were localized by electron energy loss spectroscopy mapping. Cu_2O grows as distinct crystallites on the surface of $Li_xCu_{1-x}O$ instead of forming a dense layer. Additionally, there is no obvious Cu_2O gradient inside the films, as Cu_2O seems to form on all $Li_xCu_{1-x}O$ nanocrystals exposed to water. The application of a thin $Ti_{0.8}Nb_{0.2}O_x$ coating by atomic layer deposition and the deposition of a platinum co-catalyst increased the stability of $Li_xCu_{1-x}O$ against decomposition. These devices showed a stable hydrogen evolution for 15 minutes.

Introduction

Events like the Paris agreement in the year 2015 again demonstrate the desire of our modern society to reduce emissions caused by fossil fuels. Consequently, the focus on research for sustainable energy sources has been increasing in recent years. Compared to wind power, hydroelectric power and tidal power plants, sunlight is by far the most prominent energy source we can exploit to meet mankind's rising demands.[1] An additional challenge beside harvesting sunlight and converting it into electricity is large scale energy storage, which is essential for the replacement of fossil fuels. One approach to address this demanding task is the use of hydrogen gas for powering both fuel cells and fertilizer production, envisioning the establishment of a so called 'hydrogen society'. Inspired by photosynthesis, photoelectrochemical (PEC) water splitting is a promising process to generate hydrogen and oxygen gas.[2-5] While there is lively discussion on the subject, potential advantages of a photoelectrochemical cell compared to the combination of an electrolyzer with a conventional solar cell can be the reduction of overpotentials as well as reduced fabrication cost and complexity of the final devices.[5, 6] In contrast to photocatalysis, oxygen and hydrogen are produced in spatially separated compartments, hence avoiding subsequent separation, facilitating their storage and preventing the accumulation of an explosive gas mixture. Suitable semiconducting materials for PEC cathodes are based on silicon[6-9], metal oxides[3, 5] or organic semiconductors.[10-12] Many earth abundant metal oxides are known to exhibit reasonable stability as well as photoactivity in water splitting applications.[13-15] This led to the development of synthesis methods for novel binary[16-19] and ternary[20, 21] metal oxides as well as doping of well-known metal oxides.[22-24] Besides the extensive work on materials with optical bandgaps in the range of 2.0 – 3.0 eV,[14, 15, 24-26] there is also need for low band gap photoabsorbers in order to build efficient PEC tandem cells. Such devices consist of an *n*-type photoanode connected to a *p*-type photocathode to harvest a substantial portion of the solar spectrum, reaching theoretical solar-to-hydrogen

[a] *Department of Chemistry and Center for NanoScience (CeNS), Ludwig-Maximilians-Universität München, Butenandtstr. 5-13 (E), 81377 Munich, Germany*
[b] *Max Planck Institute for Solid State Research, Heisenbergstr. 1, 70569 Stuttgart, Germany*
[c] *Universität Duisburg-Essen, Department of Physics, Forsthausweg 2, 47057 Duisburg, Germany*
[d] *Department of Chemistry, Technical University of Munich, Lichtenbergstr. 4, 85748 Garching, Germany*
[e] *Max-Planck-Institut für Eisenforschung GmbH, Max-Planck-Straße 1, 40237 Düsseldorf, Germany*
[f] *Forschungszentrum Jülich GmbH, Institute of Energy and Climate Research (IEK-1) Materials Synthesis and Processing, Wilhelm-Johnen-Straße, 52425 Jülich, Germany*

** corresponding authors*
Electronic Supplementary Information (ESI) available: [details of any supplementary information available should be included here]. See DOI: 10.1039/x0xx00000x

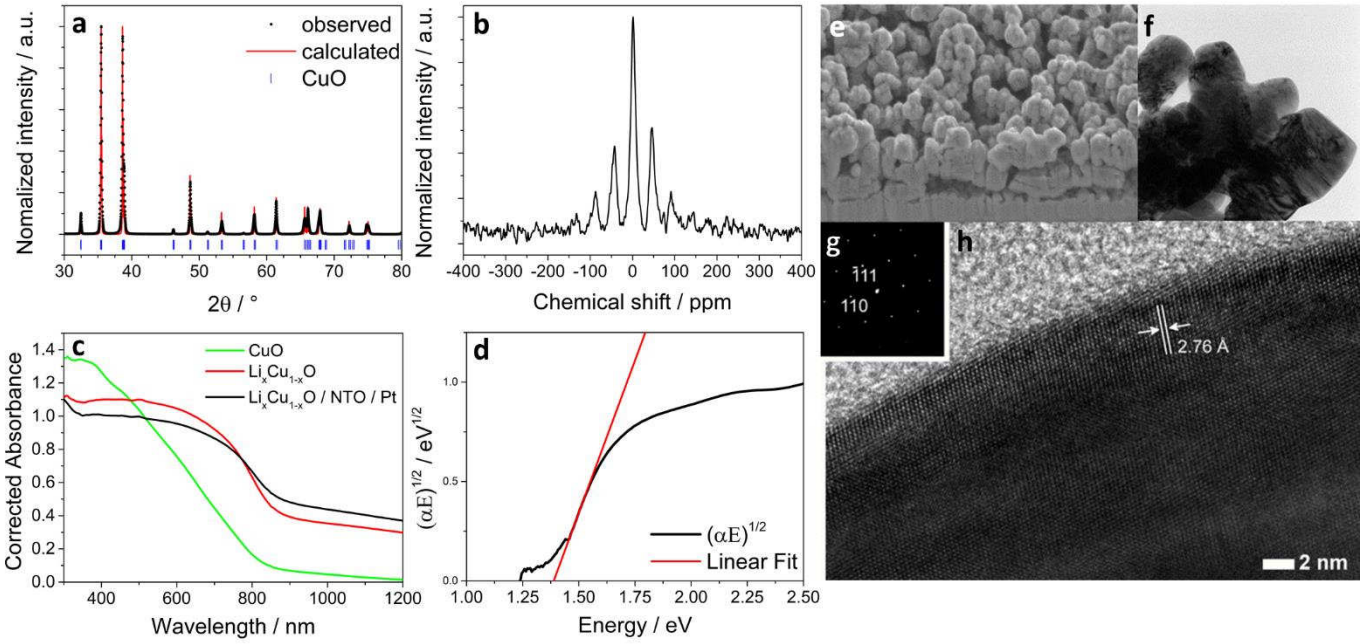

Fig. 1 a) Rietveld refinement of $Li_xCu_{1-x}O$ with observed data (·) and calculated pattern (red line), blue vertical bars mark the positions of the diffraction lines of CuO (tenorite). b) ^{7}Li-NMR spectra of $Li_xCu_{1-x}O$ showing a multiplet centered at 1.3 ppm. c) UV-Vis absorption spectrum of undoped CuO (green), $Li_xCu_{1-x}O$ (red) and protected $Li_xCu_{1-x}O$/NTO/Pt films on FTO. d) Tauc plot of a $Li_xCu_{1-x}O$ film on FTO showing an indirect bandgap of 1.39 eV. e) SEM cross section image of $Li_xCu_{1-x}O$. f) TEM image of $Li_xCu_{1-x}O$ particles. g, h) High-resolution TEM image of a highly crystalline $Li_xCu_{1-x}O$ nanoparticle and its corresponding electron diffraction pattern.

conversion efficiencies up to 21.6%.[5, 25, 27] Copper oxide based photocathodes have aroused broad interest due to their low toxicity and the good availability of copper based compounds.[22, 28-34] The reported band gaps of 1.35 eV– 1.7 eV and 2.0 – 2.2 eV for CuO and Cu_2O respectively, allow for significant light absorption in the visible range and provide enough energy for photoelectrochemical reactions.[35-39] The conduction band edges of the intrinsic p-type semiconductors CuO and Cu_2O[36, 37] fit both the reduction potentials of water[14, 38] and CO_2[40], which enables the reduction of these reagents by photo-generated electrons. The incorporation of Al or Pd into the structure of cupric oxide was shown to increase both the photocorrosion stability and the performance of those devices significantly.[41, 42] Besides this, doping CuO with Li has already been proven to be a suitable way to lower the optical band gap and increase the electrical conductivity,[22, 23, 35, 43] which is key to enhance its performance for photoelectrochemical water splitting applications. Therefore, the photoelectrochemical study solely covers results on Li doped CuO and does not compare it with undoped CuO. Several groups have reported the discovery of highly efficient photocathodes based on CuO.[22, 33, 44-47] However, it has been observed that photocurrents may be easily misinterpreted as evidence for hydrogen evolution which should be critically scrutinized.[44-46] On the other hand, also justified doubts exist already about the stability of this metal oxide under reductive potentials.[48, 49] High cathodic dark currents and a significant decay in performance within the first minutes under operating conditions could point towards cathodic corrosion of this photoabsorber.[35, 50, 51] The reduction potential of CuO in aqueous electrolyte lies above the reduction potential of water.[29] This implies the possibility of a competitive reduction of water and the photoabsorber itself, leading to the formation of reduced copper species such as Cu_2O and metallic copper under operating conditions, and consequently to a significant change of the photocathode morphology due to photocorrosion.[49, 52, 53] Other copper containing photocathode materials like Cu_2O,[14, 54] $CuFeO_2$[17] and $CuBi_2O_4$[19] are also affected by photocorrosion, which further motivated us to investigate this phenomenon in detail. Recently, more detailed corrosion studies on CuO[55] and $BiVO_4$[56-58] concentrated on the mechanisms behind the loss in activity and addressed this by the use of protective layers and suitable cocatalysts. Here, we report on the first extensive photocorrosion study revealing detailed insights into the transformations taking place in copper (II) oxide thin film electrodes under operating conditions with special attention to the role of photo-induced electrons, which we propose to be applicable to various copper containing cathode materials used in photoelectrochemical measurements. We further describe a suitable approach to increase the stability of this *p*-type low bandgap semiconductor against decomposition and to decorate it with a Pt cocatalyst. With these results, we wish to contribute to the ongoing discussion about the stability of metal oxide photocathodes and point to ways towards the development of stable photoabsorbers for the generation of environmentally friendly hydrogen gas. Furthermore, we want to present a convenient method to manipulate the electronic structure of copper oxide which can be used to improve CO_2 reduction efficiencies.

Results and Discussion

$Li_xCu_{1-x}O$ photocathode layers were prepared by spin coating an ethanolic solution of $Cu(NO_3)_2 \cdot 3\ H_2O$ and $LiNO_3$ onto an FTO substrate. Calcination of these coatings at 400°C resulted in

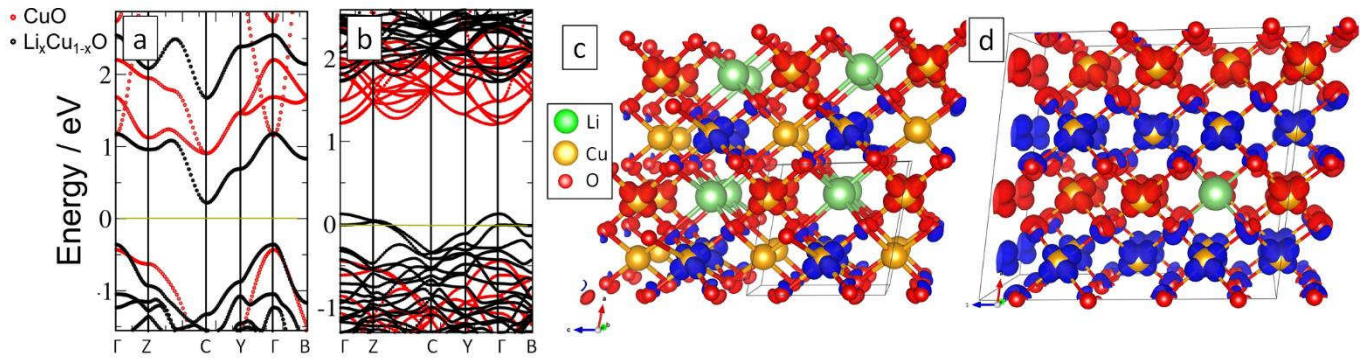

Fig. 2 Electronic band structure of lithium doped CuO for two different Li concentrations of (a) $Li_{0.25}Cu_{0.75}O$ and (b) $Li_{0.032}Cu_{0.968}O$. The different numbers of bands are related to different cell sizes. The yellow line marks the Fermi level. In contrast to the insulating behaviour for x_{Li}=25% (note the reduced band gap w.r.t. bulk CuO), the valence bands crossing the Fermi level for x_{Li}=3.2% indicate p-type conductivity. Spin density of lithium doped CuO in two different Li concentrations of (c) $Li_{0.25}Cu_{0.75}O$ and (d) $Li_{0.032}Cu_{0.968}O$ (Isosurface of 0.01 e/Å^3). Majority and minority spin densities are shown by blue and red, respectively. Note the significant contribution of oxygen for the low Li doping concentration of 3.2%.

homogeneous black films with a thickness of about 1 µm. The calcined films obtained from the precursor solution contain large amounts of non-reacted $LiNO_3$ and Li_2CO_3 (**ESI Fig. 1**) which can be removed by rinsing with water. X-ray diffraction (XRD) analysis (**Fig. 1a**) reveals that the films are structurally closely related to the CuO tenorite phase (space group: *C2/c*, a = 4.6803(8) Å; b = 3.4176(2) Å; c = 5.1278(8) Å; β = 99.442 (1)° (**ESI Fig. 2**))[59, 60] but exhibit slightly larger unit cell parameters (*a* = 4.6975(8) Å, *b* = 3.4346(6) Å, *c* = 5.1400(3) Å and β = 99.499(6)°). The small increase of the unit cell volume from 82.02(1) Å^3 for the pure CuO to 82.93(1) Å^3 for the CuO synthesized in the presence of Li salts indicates the incorporation of a small amount of Li^+ ions, with a somewhat bigger ionic radius of 0.90 Å (in CN = 6) compared to the ionic radius of Cu^{2+} ions of 0.87 Å (in CN = 6), into the crystal lattice.[23] Inductively coupled plasma atomic absorption spectroscopy (ICP-AAS) analysis confirms the presence of 4 at% Lithium in the sample, which is the maximum amount that can be incorporated in the tenorite crystal structure.[61]

Another evidence for the incorporation of Li in the structure is provided by solid state ^{7}Li nuclear magnetic resonance (NMR) analysis, which shows a multiplet (from spinning sidebands) centered at 1.3 ppm in the spectrum of a carefully washed $Li_xCu_{1-x}O$ powder (**Fig. 1b**). This signal is indicative for a non-metallic single phase, free of contaminations with diamagnetic compounds (i.e. Li_2O, $LiCO_3$, $LiNO_3$). The electrical conductivity of Li-doped CuO was determined by Hall measurements (van der Pauw method) to be 6.0 • 10^{-3} S cm^{-1}, which is an increase by a factor of 2.5 compared to undoped CuO (2.4 • 10^{-3} S cm^{-1}). While films of undoped CuO are of dark brown color, films of $Li_xCu_{1-x}O$ are black. We attribute this observation to the formation of in-gap states, which can be caused by the introduction of point defects like cation doping or oxygen vacancies.[62] These optical properties were investigated by UV-Vis spectroscopy. $Li_xCu_{1-x}O$ films demonstrate favorable light harvesting efficiencies across a broad wavelength range between 350 - 800 nm, covering part of the near infra-red (IR) range, which exceeds that of our undoped CuO films (**Fig. 1c**). Absorbance data of $Li_xCu_{1-x}O$ films were used to calculate an indirect optical bandgap of 1.39 eV via Tauc plot analysis[63] (**Fig. 1d**), which is nearly the theoretical optimum for bottom materials used for high-efficiency PEC tandem cells.[27] The morphology of our $Li_xCu_{1-x}O$ films was investigated by scanning electron microscopy (SEM, **Fig. 1e**). The films are nanostructured and composed of interconnected nanoparticles forming disordered porous layers covering the whole FTO substrate. Transmission electron microscopy (TEM) images of $Li_xCu_{1-x}O$ films reveal that they are composed of intergrown particles with a size of around 150 - 300 nm (**Fig. 1f**). High-resolution TEM (HR-TEM) images (**Fig. 1h**) and electron diffraction analysis (**Fig. 1g**) reveal that these particles are single crystalline. The $d_{(110)}$-spacing of monoclinic $Li_xCu_{1-x}O$ was determined to be 2.76 Å, being in good agreement with the XRD patterns.

To understand how the introduction of Li influences the electronic properties of CuO, we have performed density functional theory (DFT) calculations for Li-containing CuO including static electronic correlations within the GGA+U approach where the rotationally invariant formulation of Dudarev et al.[64] was employed (see supporting information for further details). We have investigated the band gap as a function of the Hubbard U parameter and find that up to U = 8 eV the indirect band gap of CuO increases monotonically with the band gap reaching 1.46 eV. Beyond U of 8 eV it changes to a direct band gap of 2.1 eV (**ESI Fig. 3a**). The band gap of 1.46 eV obtained for U = 8 eV is in good agreement with the band gap of 1.39 eV determined from the Tauc plot above and consistent with previous LDA+U studies with a somewhat lower value of U = 6.5 eV by Heinemann et al.[37] The variation of lattice constants as a function of U is presented in **ESI Fig. 3b**. The DFT predictions are in overall agreement with experimental lattice constants. The jump occurring between U = 8 eV and U = 8.5 eV is associated with the above-mentioned transition from indirect to direct band gap. To determine the preferential position of Li atoms in the CuO structure we have calculated the solution energy of Li at different lattice positions. For substitutional doping of Cu and O sites the calculated values are -4.20 eV and 1.04 eV, respectively, while for the interstitial doping the solution energy was determined to be-0.025 eV. Therefore, we can conclude that thermodynamically the preferred

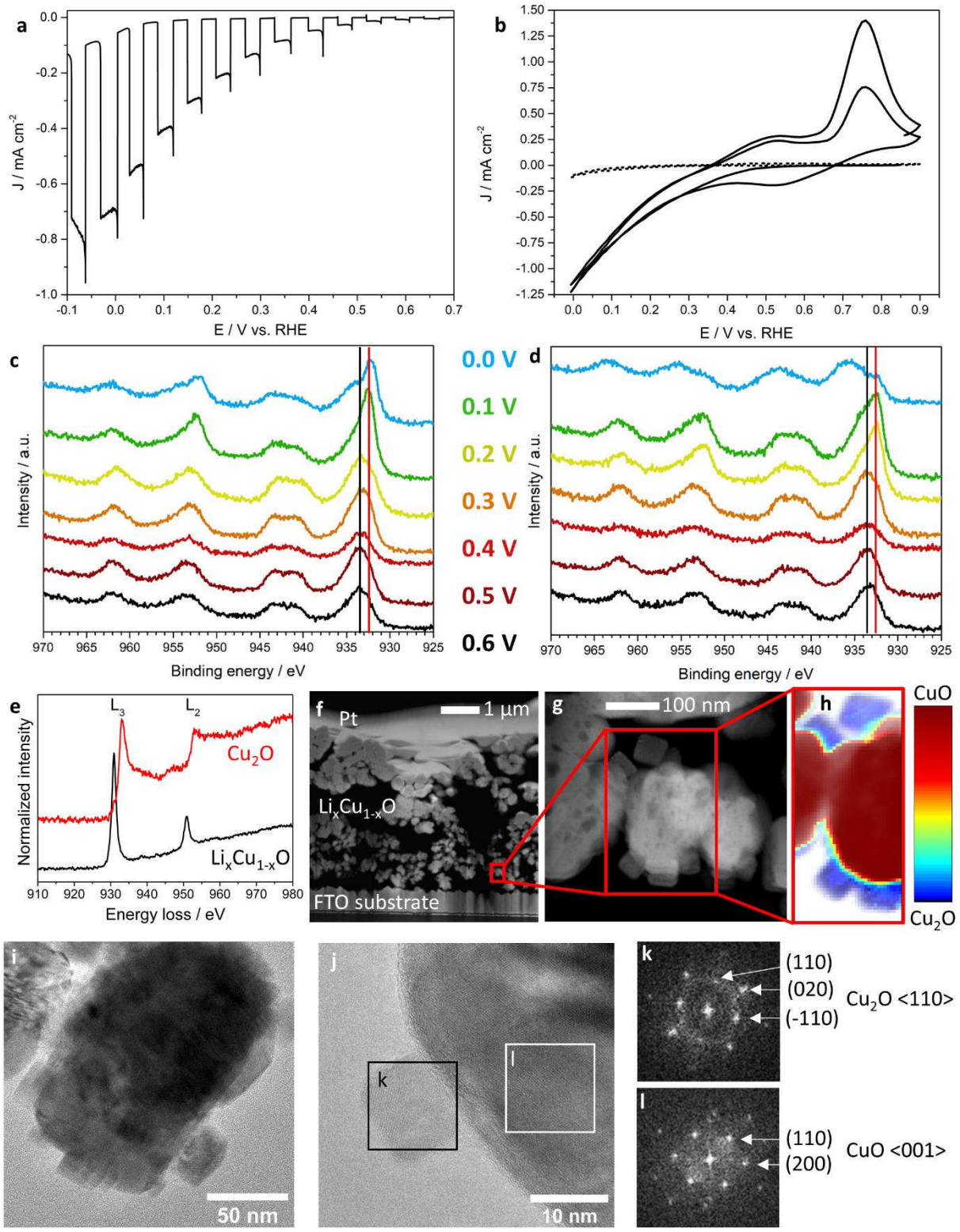

Fig. 3 . a) Linear sweep voltammogram of a bare $Li_xCu_{1-x}O$ film under chopped AM 1.5 illumination, showing no signs of photocorrosion. The assumption of a working photocathode based on this experiment is very misleading, as the reductive currents originate from both water reduction and photocorrosion. b) Cyclic voltammetry characterization of an unprotected $Li_xCu_{1-x}O$ photocathode in 0.1 M Na_2SO_4 at pH 7 in the dark (dashed line) and under AM 1.5 illumination through the substrate (solid line). c, d) Cu 2p XPS spectra measured of bare $Li_xCu_{1-x}O$ films held at the respective potentials vs. RHE for 15 minutes each in the dark (c) and under AM1.5G illumination (d) (bars: black: Cu^{2+}, red: Cu^0 and Cu^{1+}). At a potential of 0.2 V vs. RHE, $Li_xCu_{1-x}O$ is stable in the dark but corrodes to Cu_2O under illumination. e) Cu-$L_{2,3}$ edges of CuO and Cu_2O distinguish between both copper oxidation states. The photocorrosion could be localized in a TEM cross section image (f, g) with corresponding EELS map (h), showing cubic Cu_2O crystals on the $Li_xCu_{1-x}O$ surface. i) Overview image of one crystal scratched from a $Li_xCu_{1-x}O$ film after an electrochemistry experiment performed for 15 min at 0.2 V under illumination, showing a roundish crystal overgrown by square crystals. (j) Average Background Subtraction Filtered (ABSF) high resolution TEM image showing one square crystal at the surface of a spherical one. The FFTs of the marked regions were indexed for Cu_2O (k) and CuO (l), respectively.

configuration corresponds to the substitutional doping of Cu sites with Li atoms. Consequently, we postulate the delocalization of holes throughout the structure and a partial change of the copper oxidation state from Cu^{2+} to Cu^{3+} to maintain charge neutrality. The band structure of bulk $Li_xCu_{1-x}O$ was calculated for a high lithium content of x_{Li} = 25 at% and a low content of x_{Li} = 3.2 at%, which is close to the experimentally determined Li level of ca. 4 at%. The band structure of $Li_xCu_{1-x}O$ (**Fig. 2a** and **b**) shows a very strong dependence of the amount of introduced Li. While for high concentration the band gap is strongly decreased to 0.64 eV, for low concentration the main effect is an upward shift of the valence band maximum that gets closer to the Fermi level and makes the system a *p*-type semiconductor. As shown in the spin density plots in **Fig. 2c** and **d**, the underlying mechanisms are distinct: for x_{Li} = 25 at% substitution of Li^+ leads to a change in charge state of one copper to Cu^{1+}, while for x_{Li} = 3.2 at% the holes are delocalized at the oxygen sites leading to a *p*-type semiconductor. The solution energies of $Li_{0.032}Cu_{0.968}O$ and $Li_{0.25}Cu_{0.75}O$ are -4.2 eV and -3.1 eV respectively, indicating a reduction with increasing Li concentration due to Li-Li repulsion. To sum up, Lithium doping causes an increased optical absorption of CuO in the infrared range and significantly increases the *p*-type conductivity, therefore we expect facilitated charge separation. As our morphology is beneficial for the strongly surface-depending water splitting reaction[5], we determined the photoelectrochemical performance of $Li_xCu_{1-x}O$ photocathodes by linear sweep voltammetry (LSV) in 0.1 M Na_2SO_4 aqueous solution (pH 7) starting at 0.7 V vs. RHE and scanning down towards -0.1 V vs. RHE under chopped AM 1.5 illumination. In the present case, the result of this procedure (**Fig. 3a**) is very misleading, as the $Li_xCu_{1-x}O$ film shows the typical behavior of a photocathode with instant photocurrent response upon illumination. This observation can easily be misinterpreted as a measure of hydrogen evolution efficiency, but indeed originates from both the reduction of water and the reduction of the transition metal oxide itself, which we elucidate in the present work. In addition, we performed cyclic voltammetry (CV) measurements in a potential range between 0.0 and 0.9 V vs. RHE (**Fig. 3b**). The material shows a negligible dark current, indicating electrochemical stability in the scanned potential range. Under AM1.5G illumination (100 mW cm^{-2}), a reductive current density can be observed below 0.5 V vs. RHE. However, significant oxidizing currents appear above 0.4 V vs. RHE in the back scan. To examine the electrochemical stability of our $Li_xCu_{1-x}O$ photocathodes, we applied different constant potentials from 0.0 to 0.6 V vs. RHE for 15 minutes each, in the dark as well as under illumination (**ESI Fig. 7**). X-ray photoelectron spectroscopy (XPS) measurements of these films after electrochemical reaction were used to get further insights into the stability of the electrode material. From the binding energy of the Cu $2p_{3/2}$-peak (**Fig. 3c, d**), the oxidation state of the copper at the electrode surface could be assigned to Cu(II) (933.6 eV) or Cu(I) (932.4 eV).[65] As can be seen in **Fig. 3c**, copper (II) oxide remains stable without illumination down to 0.2 V vs. RHE. Below this potential a shift of the Cu $2p_{3/2}$-peak to lower binding energies is observed, indicative for the reduction of copper (II) oxide to copper (I) oxide. Under AM1.5G illumination, we observed copper (I) oxide formation already at 0.2 V vs. RHE, indicating photocorrosion by light induced electrons at this potential. Deconvolution of the Cu $2p_{3/2}$-peak as well as the corresponding Cu L_3VV Auger signals support this conclusion (**ESI Fig. 13**).

In agreement with the XPS data[65, 66] and the Pourbaix diagram of copper[67], we attribute the reductive currents to a competitive reduction of both 2 H^+ to H_2 and Cu^{2+} to Cu^{1+}, while the oxidizing currents occur from the oxidation of Cu^{1+} to Cu^{2+}.[35] Furthermore, we extended the potential range of several CV measurements stepwise on a new sample (**ESI Fig. 5**). With scanning to lower potentials, more Cu^{2+} is photoreduced to Cu^{1+}, which gets reoxidized to Cu^{2+} at 0.75 V vs. RHE. This extremely sensitive method indicates a photocorrosion onset at approximately 0.45 V vs. RHE. Notably, photocorrosion starts right with the photoelectrochemical measurement (**ESI Fig. 19**) and is fully noticeable after 15 min. Impedance plots illustrate the impairing effect of photocorrosion on the charge transport properties on the photocathode – electrolyte interface (**ESI Fig. 20**). With proceeding Cu_2O formation on the surface, we observed an increase in charge transfer resistance on $Li_xCu_{1-x}O$ electrodes.[68] We address this phenomenon to the high conduction band energy level of Cu_2O compared to CuO, which hinders electron transfer from $Li_xCu_{1-x}O$ towards the electrolyte. Electron energy loss spectroscopy (EELS) allows one to directly monitor the oxidation states of elements on the nanometer scale using the near edge fine structure. The Cu-$L_{2,3}$ edges of CuO and Cu_2O are characterized by a pair of white lines which result from the excitation of $2p_{3/2}$ (L_3) and $2p_{1/2}$ (L_2) electrons to unoccupied 3d states (**Fig. 3e**). The white lines of CuO are shifted to lower energy losses compared to Cu_2O.[69, 70] Thus, the energetic position of the two white lines was used in this study to identify the local distribution of the o xidation states in the thin films (**ESI Fig. 6**). EELS requires electron transparent samples (thickness below 100 nm),[70] which in this study was achieved by preparing thin lamellae with a focused ion beam microscope. The resulting lamella represents a cross-section through the thin film (**Fig. 3f, g**). A platinum protection layer was used to protect the sample from the gallium ions used for sample cutting and thinning. Oxidation state maps illustrate the local distribution of Cu_2O and CuO inside the thin film with the spatial resolution given by the pixel size of the map, which was commonly chosen between 2.5 and 5 nm using subpixel scanning to reduce beam damage. Both oxidation states are detected in the interfacial regions between the two phases. In the TEM images two different crystal morphologies are visible, large round crystals and smaller square crystals. The latter form preferably at the surface of the large crystals. EELS maps demonstrate that the two crystal morphologies correspond to the two oxidation states: the large crystals are pure CuO, while the smaller ones are Cu_2O (**Fig. 3h**). This is confirmed by high resolution TEM imaging of the two crystal morphologies (**Fig. 3i, j**) with their corresponding *fast Fourier transforms* (FFTs) indexed for CuO and Cu_2O (**Fig. 3k, l**). Interestingly, Cu_2O grows as distinct crystallites on the surface of CuO instead of forming

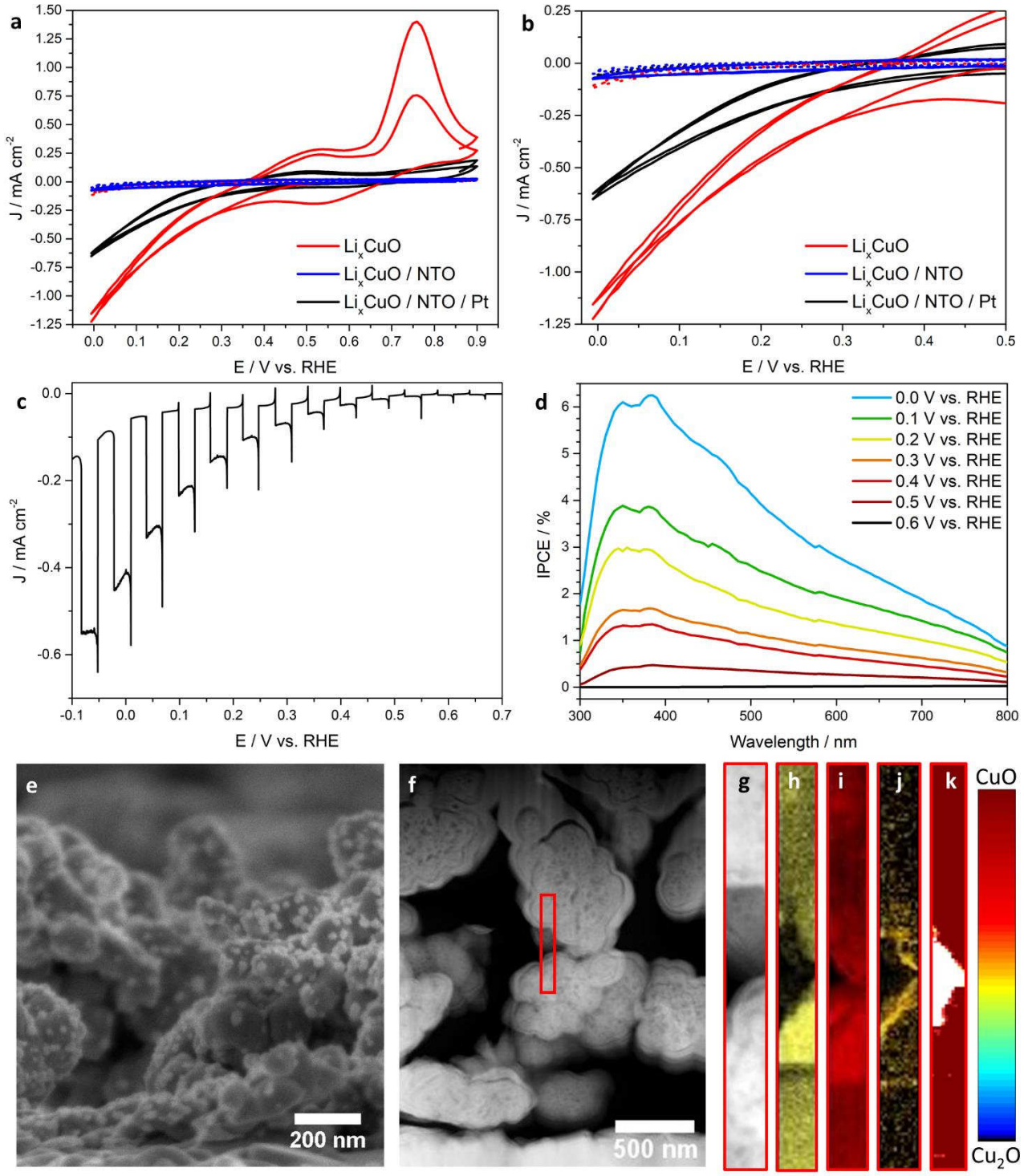

Fig. 4 a) Cyclic voltammetry measurements of $Li_xCu_{1-x}O$ films protected with 2.5 nm thin $Ti_{0.8}Nb_{0.2}O_x$ (NTO) layer (blue) and additionally functionalized with Pt nanoparticles (black) compared to a bare $Li_xCu_{1-x}O$ photocathode (red) in the dark (dashed) and under AM1.5 illumination (solid). b) Magnification of (a) in the lower potential range. c) Linear sweep voltammogram of a $Li_xCu_{1-x}O$/NTO/Pt film under chopped AM 1.5 illumination. d) Incident-photon-to-current-efficiency (IPCE) measurements at different potentials. e) SEM image of a $Li_xCu_{1-x}O$/NTO photocathode decorated with 20 nm sized Pt particles. f) STEM image of a cross section of a $Li_xCu_{1-x}O$/NTO/Pt device held for 15 min at 0.2 V vs. RHE under AM1.5 illumination. The marked area (red, g) was used for EDX mapping of Cu (h), O (i) and Ti (j). The corresponding EELS map (k) shows no sign of photocorrosion.

a dense layer on its surface. Additionally, there is no obvious Cu_2O gradient inside the films, as Cu_2O seems to form on all CuO nanocrystals exposed to water. We see a similar photocorrosion behavior on undoped CuO. After a potentiostatic measurement for 15 minutes at 0.2 V vs. RHE, also the surface of CuO is covered with cubic crystallites. Both the post-photoelectrochemical XRD pattern of CuO as well as FFTs and electron diffraction pattern of the regions covered with cubic crystals indicate the formation of the cuprite phase (Cu_2O) (**ESI Fig. 11**). Therefore, we expect the same corrosion mechanism

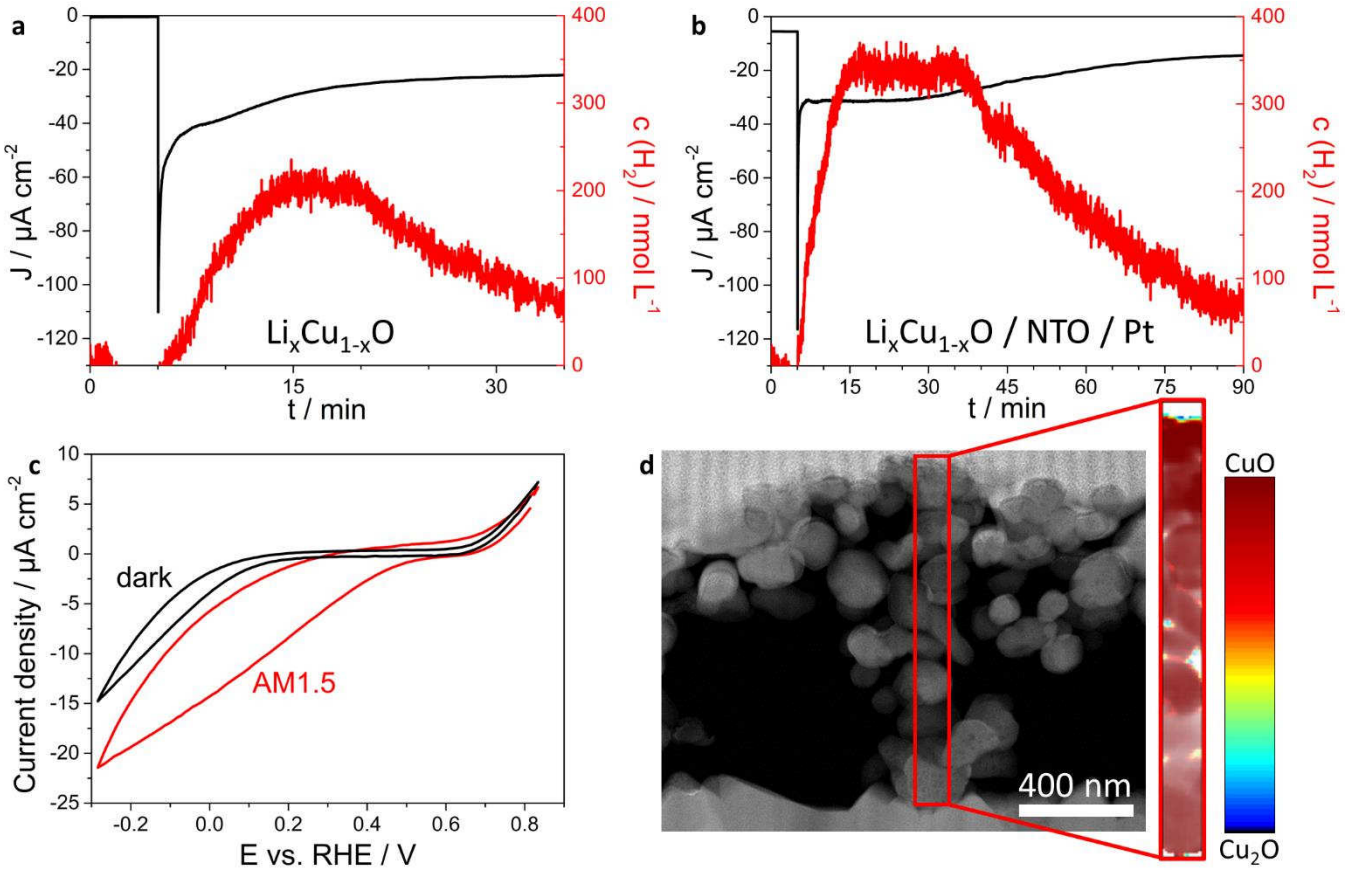

Fig. 5 a, b) Chronoamperometric data (black) at 0.3 V vs. RHE with corresponding H_2 evolution (red), which is directly correlated to illumination starting after 5 minutes. While unprotected $Li_xCu_{1-x}O$ films (a) start to degrade right after illumination, $Li_xCu_{1-x}O$/NTO/Pt photocathodes (b) show stable hydrogen evolution during the first 30 minutes. c, d) To probe the role of the water during the electrochemical reaction, a propylene carbonate electrolyte with an iodide triiodide redox couple was used as replacement. The CV measurement (c) as well as the TEM cross section with corresponding EELS map (d) of the film after a 15 minutes' stability test at 0.1 V vs. RHE show no sign of photocorrosion.

like on $Li_xCu_{1-x}O$ photocathodes. To rule out artefacts introduced by the FIB sample preparation, FIB lamellae of reference samples that had not been used in photoelectrochemical experiments were investigated. The maps show a thin layer of reduced copper oxide at the surface of the CuO crystals (see **ESI Fig. 8**), but no Cu_2O crystals. The reduction of the surface layer of CuO is most likely caused by a reaction of CuO with the Ga-ions used for the sample preparation. To stabilize our photoabsorber material, we coated our $Li_xCu_{1-x}O$ films with a protective layer by atomic layer deposition (ALD), as this is a proven approach to protect copper oxides against photocorrosion.[14, 32, 71] Among several tested coatings like TiO_2, $Ti_{0.8}Nb_{0.2}O_x$ (NTO), SnO_x, Al:ZnO and Al_2O_3, NTO exhibited the best results on our $Li_xCu_{1-x}O$ morphology. After deposition, the applied $Ti_{0.8}Nb_{0.2}O_x$ layers are amorphous (**ESI Fig. 12**),[72, 73] covering the complete surface of the nanostructured morphology of the $Li_xCu_{1-x}O$ films without the formation of pinholes (**ESI Fig. 15**), which has already been demonstrated to successfully protect Cu_2O.[54] CV measurements of $Li_xCu_{1-x}O$/NTO films in aqueous 0.1 M Na_2SO_4 are free of oxidative current signals, indicating that the photoabsorber remains stable under illumination. In contrast to bare $Li_xCu_{1-x}O$, NTO covered films showed no activity in terms of water reduction (**Fig. 4a** and **b**, blue) due to the lack of a suitable cocatalyst.[3] For this reason, we electrodeposited Pt nanoparticles on our $Li_xCu_{1-x}O$/NTO from a 1 mM methanolic H_2PtCl_6 solution (see experimental details for further information), as this is a proven way to improve HER kinetics on ALD protected copper oxide based photocathodes.[14] 20 nm sized Pt particles are formed on the surface of the nanostructured $Li_xCu_{1-x}O$/NTO films (**Fig. 4e**). A protection layer of 2.5 nm NTO showed the highest activity compared slightly thinner or thicker NTO layers, still allowing sufficient charge transport to the Pt cocatalyst (**ESI Fig. 14**). We assume electron transport by tunneling through the protective layer due to its extremely small layer thickness. The described protection strategy causes no significant change in the light absorption properties of those devices compared to the pristine $Li_xCu_{1-x}O$ films (**Fig. 1c**). We see no signs of photocorrosion of $Li_xCu_{1-x}O$/NTO/Pt devices held for 15 min at 0.2 V vs. RHE under AM1.5G illumination. This is verified by EELS oxidation state mapping (**Fig. 4f, k** and **ESI Fig. 16**). Based on LSV measurements under chopped illumination, these devices show a distinct activity towards hydrogen evolution reaching up to 350 µA cm^{-2} at 0.0 V vs. RHE with a photocurrent onset at around 0.50 V vs. RHE (**Fig. 4c**). Furthermore, we quantified the incident-photon-to-current-efficiency (IPCE) at different potentials from 0.6 to 0.0 V vs. RHE (**Fig. 4d**). The photocathode is active over the whole visible spectrum, reaching parts of the IR range, with an IPCE maximum at an excitation wavelength of 380 nm. The

IPCE increases with lower potentials, reaching up to 6.25% at 0.0 V vs. RHE.

In addition, we performed stability tests of bare $Li_xCu_{1-x}O$ and $Li_xCu_{1-x}O$/NTO/Pt films under illumination and quantified the evolved hydrogen. At a constant potential of 0.3 V vs. RHE, both photoelectrodes show a current response under illumination which is directly correlated to hydrogen evolution. The photocurrent of bare $Li_xCu_{1-x}O$ decreases constantly and the hydrogen evolution stops after around 10 min of illumination due to photocorrosion of the material (**ESI Fig. 18**), which results in a Faradaic efficiency of 61% after 10 minutes (**Fig. 5a**). In contrast, the $Li_xCu_{1-x}O$/NTO/Pt device produces a stable photocurrent and evolves hydrogen with a Faradaic efficiency of 96% during the first 15 minutes after illumination (**Fig. 5b**). Afterwards, both the hydrogen evolution and the current drop. We attribute the activity loss to the detachment of the Pt nanoparticles due to hydrogen bubble formation (see **ESI Fig. 17**), whereas the decrease of hydrogen concentration can be attributed to leakage from the photoelectrochemical cuvette-type cell used for hydrogen evolution experiments. We are currently working on the optimization of the cocatalyst deposition to increase both stability and activity of Li doped CuO photocathodes. Without direct contact to water, bare $Li_xCu_{1-x}O$ is stable in a comparable potential range, as shown in a photoelectrochemical measurement in 1 mM iodide/triioide (I^- / I_3^-) propylene carbonate electrolyte (**Fig. 5c**). No oxidative currents are detectable, which would indicate a Cu^{1+} / Cu^{2+} reaction similar to the one shown in **Fig. 3b**. Moreover, the $Li_xCu_{1-x}O$ film was held under illumination at 0.1 V vs. RHE for 15 minutes. The corresponding EELS map of this sample shows no sign of photocorrosion. From this observation, we conclude that $Li_xCu_{1-x}O$ could be used as stable photoabsorber as well as catalyst in a water-free electrolyte.

Conclusions

In this study, we have presented black Li-doped CuO thin films as cathodic light absorber for photoelectrochemical hydrogen evolution. The substitution of 4 at-% of Cu^{2+} with Li^+ ions has a substantial influence on the optical and electronic properties. The optical bandgap is reduced while both electrical conductivity and *p*-type character increase upon Li doping, which is beneficial for the application as photocathode material in a PEC tandem cell. DFT+U calculations confirm that the system becomes a *p*-type semiconductor for low Li concentrations due to the pronounced delocalization of holes. While $Li_xCu_{1-x}O$ is stable in a non-aqueous electrolyte, it suffers from photocorrosion in contact with water. For the first time, the corrosion was studied in detail by cyclic voltammetry, X-ray photoelectron and electron energy loss spectroscopy. Therefore, we presented a detailed study on photocorrosion to provide a profound understanding of the underlying physical process which will be applicable to any copper based photocatalyst. Indeed, the performance of other reported photoelectrode systems should be critically revised.

Under illumination and in direct contact with water, the reduced Cu_2O forms as distinct cubic crystals on the $Li_xCu_{1-x}O$ surface. We demonstrate that $Li_xCu_{1-x}O$ films can be stabilized to some degree against photocorrosion by using approaches common in photoelectrochemical research namely the application of a thin Nb:TiO_2 protection layer in combination with a Pt cocatalyst. Still, our described approach cannot solve the fundamental problem of intrinsic instability of metal oxide-based photocathodes in aqueous electrolytes. We suggest that similar fundamental problems of photocorrosion stability will be witnessed also in other copper containing photoabsorbers, therefore the photoelectrochemical performance and possible light-triggered material transformation should be revisited with special care. We doubt that the intrinsic photocorrosion of copper oxide based photoelectrodes can be solved in any feasible way in aqueous electrolytes. However, the *in-situ* growth of Cu_2O due to photoreduction could be used for other types of electrochemical processes. As an example, the use as specific catalyst for CO_2 reduction in a water-free, methanolic electrolyte can be envisioned as both copper oxides were already described to be very active for this application.[74] By manipulating their electronic structure using various dopants like Li^+, we expect to enhance both the efficiency of copper oxides and also fine tune the formation efficiencies for hydrocarbons like methane and ethylene.

Conflicts of interest

The authors declare no competing financial interest.

Acknowledgements

The presented work was supported by the German Research Foundation (DFG) via the SPP 1613, the Nanosystems Initiative Munich (NIM) and LMUexcellent funded by the DFG, the Bavarian research network 'Solar Technologies Go Hybrid', and the Center for Nanoscience (CeNS). Dr. Ilina Kondofersky, Dr. Markus Döblinger, Dr. Steffen Schmidt, Dr. Andreas Wisnet and Dr. Ramona Hoffmann are gratefully acknowledged for insightful discussions and help with the FIB and TEM measurements. We thank the students Leonard Moser and Jan Heinemann who participated in the research. We acknowledge computational time at SuperMUC of Leibniz Rechenzentrum, grant pr87ro.

References

1. *Basic research needs for solar energy utilization*, Office of Basic Energy Sciences, US Department of Energy, 2005.
2. L. Fornarini, A. J. Nozik and B. A. Parkinson, *The Journal of Physical Chemistry*, 1984, **88**, 3238-3243.
3. A. Heller, *Science*, 1984, **223**, 1141-1148.
4. M. G. Walter, E. L. Warren, J. R. McKone, S. W. Boettcher, Q. Mi, E. A. Santori and N. S. Lewis, *Chem Rev*, 2010, **110**, 6446-6473.
5. R. van de Krol, Y. Liang and J. Schoonman, *Journal of Materials Chemistry*, 2008, **18**, 2311.
6. O. Khaselev, *International Journal of Hydrogen Energy*, 2001, **26**, 127-132.
7. R. N. Dominey, N. S. Lewis, J. A. Bruce, D. C. Bookbinder and M. S. Wrighton, *Journal of the American Chemical Society*, 1982, **104**, 467-482.
8. U. Sim, T.-Y. Yang, J. Moon, J. An, J. Hwang, J.-H. Seo, J. Lee, K. Y. Kim, J. Lee, S. Han, B. H. Hong and K. T. Nam, *Energy & Environmental Science*, 2013, **6**, 3658-3664.

9. Y. Hou, B. L. Abrams, P. C. Vesborg, M. E. Bjorketun, K. Herbst, L. Bech, A. M. Setti, C. D. Damsgaard, T. Pedersen, O. Hansen, J. Rossmeisl, S. Dahl, J. K. Norskov and I. Chorkendorff, *Nat Mater*, 2011, **10**, 434-438.
10. T. Sick, A. G. Hufnagel, J. Kampmann, I. Kondofersky, M. Calik, J. M. Rotter, A. Evans, M. Doblinger, S. Herbert, K. Peters, D. Bohm, P. Knochel, D. D. Medina, D. Fattakhova-Rohlfing and T. Bein, *J Am Chem Soc*, 2018, **140**, 2085-2092.
11. M. Haro, C. Solis, G. Molina, L. Otero, J. Bisquert, S. Gimenez and A. Guerrero, *The Journal of Physical Chemistry C*, 2015, **119**, 6488-6494.
12. T. Bourgeteau, D. Tondelier, B. Geffroy, R. Brisse, S. Campidelli, R. Cornut and B. Jousselme, *Journal of Materials Chemistry A*, 2016, **4**, 4831-4839.
13. R. Sathre, C. D. Scown, W. R. Morrow, J. C. Stevens, I. D. Sharp, J. W. Ager, K. Walczak, F. A. Houle and J. B. Greenblatt, *Energy Environ. Sci.*, 2014, **7**, 3264-3278.
14. A. Paracchino, V. Laporte, K. Sivula, M. Gratzel and E. Thimsen, *Nat Mater*, 2011, **10**, 456-461.
15. K. Sivula, F. Le Formal and M. Gratzel, *ChemSusChem*, 2011, **4**, 432-449.
16. R. Patil, S. Kelkar, R. Naphade and S. Ogale, *J. Mater. Chem. A*, 2014, **2**, 3661-3668.
17. M. S. Prevot, N. Guijarro and K. Sivula, *ChemSusChem*, 2015, **8**, 1359-1367.
18. U. A. Joshi, A. M. Palasyuk and P. A. Maggard, *The Journal of Physical Chemistry C*, 2011, **115**, 13534-13539.
19. S. P. Berglund, F. F. Abdi, P. Bogdanoff, A. Chemseddine, D. Friedrich and R. van de Krol, *Chemistry of Materials*, 2016, **28**, 4231-4242.
20. I. Kondofersky, A. Muller, H. K. Dunn, A. Ivanova, G. Stefanic, M. Ehrensperger, C. Scheu, B. A. Parkinson, D. Fattakhova-Rohlfing and T. Bein, *J Am Chem Soc*, 2016, **138**, 1860-1867.
21. K. Sliozberg, H. S. Stein, C. Khare, B. A. Parkinson, A. Ludwig and W. Schuhmann, *ACS Appl Mater Interfaces*, 2015, **7**, 4883-4889.
22. C.-Y. Chiang, Y. Shin and S. Ehrman, *Energy Procedia*, 2014, **61**, 1799-1802.
23. C.-Y. Chiang, Y. Shin and S. Ehrman, *Journal of The Electrochemical Society*, 2011, **159**, B227-B231.
24. H. K. Dunn, J. M. Feckl, A. Muller, D. Fattakhova-Rohlfing, S. G. Morehead, J. Roos, L. M. Peter, C. Scheu and T. Bein, *Phys Chem Chem Phys*, 2014, **16**, 24610-24620.
25. L. M. Peter, *J Solid State Electrochem*, 2012, **17**, 315-326.
26. A. L. Linsebigler, G. Lu and J. T. Yates, *Chemical Reviews*, 1995, **95**, 735-758.
27. M. S. Prévot and K. Sivula, *The Journal of Physical Chemistry C*, 2013, **117**, 17879-17893.
28. Y. Yang, D. Xu, Q. Wu and P. Diao, *Scientific Reports*, 2016, **6**, 35158.
29. U. Shaislamov and H.-J. Lee, *Journal of the Korean Physical Society*, 2016, **69**, 1242-1246.
30. U. Shaislamov, K. Krishnamoorthy, S. J. Kim, A. Abidov, B. Allabergenov, S. Kim, S. Choi, R. Suresh, W. M. Ahmed and H.-J. Lee, *International Journal of Hydrogen Energy*, 2016, **41**, 2253-2262.
31. P. Basnet and Y. Zhao, *Catalysis Science & Technology*, 2016, **6**, 2228-2238.
32. Y. F. Lim, C. S. Chua, C. J. Lee and D. Chi, *Phys Chem Chem Phys*, 2014, **16**, 25928-25934.
33. C.-Y. Chiang, Y. Shin, K. Aroh and S. Ehrman, *International Journal of Hydrogen Energy*, 2012, **37**, 8232-8239.
34. D. Barreca, P. Fornasiero, A. Gasparotto, V. Gombac, C. Maccato, T. Montini and E. Tondello, *ChemSusChem*, 2009, **2**, 230-233.
35. F. P. Koffyberg and F. A. Benko, *Journal of Applied Physics*, 1982, **53**, 1173-1177.
36. B. K. Meyer, A. Polity, D. Reppin, M. Becker, P. Hering, P. J. Klar, T. Sander, C. Reindl, J. Benz, M. Eickhoff, C. Heiliger, M. Heinemann, J. Bläsing, A. Krost, S. Shokovets, C. Müller and C. Ronning, *physica status solidi (b)*, 2012, **249**, 1487-1509.
37. M. Heinemann, B. Eifert and C. Heiliger, *Physical Review B*, 2013, **87**, 115111.
38. D. Chauhan, V. Satsangi, S. Dass and R. Shrivastav, *Bulletin of Materials Science*, 2006, **29**, 709.
39. L. C. Olsen, R. C. Bohara and M. W. Urie, *Applied Physics Letters*, 1979, **34**, 47-49.
40. X. Ba, L.-L. Yan, S. Huang, J. Yu, X.-J. Xia and Y. Yu, *The Journal of Physical Chemistry C*, 2014, **118**, 24467-24478.
41. S. Masudy-Panah, Y. J. K. Eugene, N. D. Khiavi, R. Katal and X. Gong, *Journal of Materials Chemistry A*, 2018, **6**, 11951-11965.
42. S. Masudy-Panah, R. Katal, N. D. Khiavi, E. Shekarian, J. Hu and X. Gong, *Journal of Materials Chemistry A*, 2019, **7**, 22332-22345.
43. P. Chand, A. Gaur, A. Kumar and U. Kumar Gaur, *Applied Surface Science*, 2014, **307**, 280-286.
44. S. Masudy-Panah, R. S. Moakhar, C. S. Chua, A. Kushwaha, T. I. Wong and G. K. Dalapati, *RSC Advances*, 2016, **6**, 29383-29390.
45. Y. J. Jang, J. W. Jang, S. H. Choi, J. Y. Kim, J. H. Kim, D. H. Youn, W. Y. Kim, S. Han and J. Sung Lee, *Nanoscale*, 2015, **7**, 7624-7631.
46. Z. Zhang and P. Wang, *J. Mater. Chem.*, 2012, **22**, 2456-2464.
47. C.-Y. Chiang, K. Aroh, N. Franson, V. R. Satsangi, S. Dass and S. Ehrman, *International Journal of Hydrogen Energy*, 2011, **36**, 15519-15526.
48. C.-M. Wang and C.-Y. Wang, *NANOP*, 2014, **8**, 084095-084095.
49. X. Guo, P. Diao, D. Xu, S. Huang, Y. Yang, T. Jin, Q. Wu, M. Xiang and M. Zhang, *International Journal of Hydrogen Energy*, 2014, **39**, 7686-7696.
50. L. Chen, S. Shet, H. Tang, H. Wang, T. Deutsch, Y. Yan, J. Turner and M. Al-Jassim, *Journal of Materials Chemistry*, 2010, **20**, 6962-6967.
51. C.-Y. Chiang, M.-H. Chang, H.-S. Liu, C. Y. Tai and S. Ehrman, *Industrial & Engineering Chemistry Research*, 2012, **51**, 5207-5215.
52. S. Emin, F. F. Abdi, M. Fanetti, W. Peng, W. Smith, K. Sivula, B. Dam and M. Valant, *Journal of Electroanalytical Chemistry*, 2014, **717-718**, 243-249.
53. H. Choi and M. Kang, *International Journal of Hydrogen Energy*, 2007, **32**, 3841-3848.
54. A. Paracchino, N. Mathews, T. Hisatomi, M. Stefik, S. D. Tilley and M. Grätzel, *Energy & Environmental Science*, 2012, **5**, 8673-8681.
55. H. Xing, L. E, Z. Guo, D. Zhao, X. Li and Z. Liu, *Inorganic Chemistry Frontiers*, 2019, **6**, 2488-2499.
56. S. Zhang, M. Rohloff, O. Kasian, A. M. Mingers, K. J. J. Mayrhofer, A. Fischer, C. Scheu and S. Cherevko, *The Journal of Physical Chemistry C*, 2019, **123**, 23410-23418.
57. F. M. Toma, J. K. Cooper, V. Kunzelmann, M. T. McDowell, J. Yu, D. M. Larson, N. J. Borys, C. Abelyan, J. W. Beeman, K. M. Yu, J. Yang, L. Chen, M. R. Shaner, J. Spurgeon, F. A. Houle, K. A. Persson and I. D. Sharp, *Nat Commun*, 2016, **7**, 12012.
58. D. K. Lee and K.-S. Choi, *Nature Energy*, 2017, **3**, 53-60.
59. G. Tunell, E. Posnjak and C. Ksanda, *Zeitschrift für Kristallographie-Crystalline Materials*, 1935, **90**, 120-142.
60. P. Niggli, *Zeitschrift für Kristallographie-Crystalline Materials*, 1922, **57**, 253-299.
61. P. Carretta, M. Corti and A. Rigamonti, *Phys Rev B Condens Matter*, 1993, **48**, 3433-3444.
62. C. Baeumer, C. Funck, A. Locatelli, T. O. Mentes, F. Genuzio, T. Heisig, F. Hensling, N. Raab, C. M. Schneider, S. Menzel, R. Waser and R. Dittmann, *Nano Lett*, 2019, **19**, 54-60.
63. D. Roy, G. F. Samu, M. K. Hossain, C. Janáky and K. Rajeshwar, *Catalysis Today*, 2018, **300**, 136-144.
64. S. L. Dudarev, G. A. Botton, S. Y. Savrasov, C. J. Humphreys and A. P. Sutton, *Physical Review B*, 1998, **57**, 1505-1509.
65. M. C. Biesinger, L. W. M. Lau, A. R. Gerson and R. S. C. Smart, *Applied Surface Science*, 2010, **257**, 887-898.
66. S. Poulston, P. M. Parlett, P. Stone and M. Bowker, *Surface and Interface Analysis*, 1996, **24**, 811-820.
67. B. Beverskog and I. Puigdomenech, *Journal of The Electrochemical Society*, 1997, **144**, 3476-3483.
68. S. Masudy-Panah, R. Siavash Moakhar, C. S. Chua, H. R. Tan, T. I. Wong, D. Chi and G. K. Dalapati, *ACS Appl Mater Interfaces*, 2016, **8**, 1206-1213.
69. L. Laffont, M. Y. Wu, F. Chevallier, P. Poizot, M. Morcrette and J. M. Tarascon, *Micron*, 2006, **37**, 459-464.
70. R. D. Leapman, L. A. Grunes and P. L. Fejes, *Physical Review B*, 1982, **26**, 614-635.
71. J. Azevedo, S. D. Tilley, M. Schreier, M. Stefik, C. Sousa, J. P. Araújo, A. Mendes, M. Grätzel and M. T. Mayer, *Nano Energy*, 2016, **24**, 10-16.
72. V. Pore, M. Ritala, M. Leskelä, T. Saukkonen and M. Järn, *Crystal Growth & Design*, 2009, **9**, 2974-2978.
73. A. G. Hufnagel, S. Haringer, M. Beetz, B. Boller, D. Fattakhova-Rohlfing and T. Bein, *Nanoscale*, 2019, **11**, 14285-14293.
74. S. Ohya, S. Kaneco, H. Katsumata, T. Suzuki and K. Ohta, *Catalysis Today*, 2009, **148**, 329-334.